



# Brönsted acid site regulates local electronic structure and O<sub>2</sub> adsorption mode of nitrogen vacancy in carbon nitride for enhanced photocatalysis

Cailiang Yue<sup>a</sup>, Linlin Zhu<sup>a</sup>, Nan Sun<sup>a</sup>, Zhiling Du<sup>a</sup>, Changqing Zhu<sup>a,b,\*</sup>, Fuqiang Liu<sup>a,\*\*</sup>

<sup>a</sup> State Key Laboratory of Pollution and Resource Reuse, School of the Environment, Nanjing University, Nanjing 210023, PR China

<sup>b</sup> Nanjing Institute of Environmental Science, Ministry of Ecology and Environment of the People's Republic of China, PR China

## ARTICLE INFO

### Keywords:

Photocatalytic O<sub>2</sub> activation  
Antibiotics degradation  
Nitrogen vacancy  
Brönsted acid site  
Carbon nitride

## ABSTRACT

This work reported an ultra-thin carbon nitride (UCN-H) with both Brönsted acid sites and nitrogen vacancies (N<sub>V</sub>) for rapid antibiotics degradation via photocatalytic O<sub>2</sub> activation. Taking guanidinium isothiocyanate as the precursor, the Brönsted acid sites were modified near N<sub>V</sub> via a two-step pyrolysis strategy, thus greatly improving e<sup>-</sup>-h<sup>+</sup> separation efficiency and O<sub>2</sub> adsorption capacity. UCN-H could produce abundant •O<sub>2</sub> and h<sup>+</sup> under simulated solar light for tetracycline with the kinetic rate constant reaching 0.3783 min<sup>-1</sup>, exceeding those of reported photocatalysts by 8–130 times. Theoretical calculations revealed that Brönsted acid sites not only increased the local electron density of N<sub>V</sub>, but also stabilized the structure of N<sub>V</sub> by forming intramolecular N-H-N hydrogen bond, so that O<sub>2</sub> could be adsorbed on N<sub>V</sub> in bridging mode rather than side-on mode. This significantly increased O<sub>2</sub> adsorption energy and electron transfer amount from N<sub>V</sub>, thus realizing highly efficient O<sub>2</sub> activation.

## 1. Introduction

The abuse of antibiotics has posed a serious threat to the ecological environment, which would harm mankind itself in return [1,2]. Owing to the non-biodegradable property, antibiotics in water cannot be effectively removed by conventional activated sludge process [3]. In recent years, advanced oxidation processes (AOPs) have been proved to be efficient strategies to eliminate refractory antibiotics. Commonly, AOPs can utilize the reactive oxygen species (ROS) to realize the degradation and mineralization of organic pollutants, which are generated via the activation of oxidants, including ozone [4,5], hydrogen peroxide [6,7], persulphate [8,9], peroxymonosulphate [10,11], periodate [12,13] and peracetic acid [14,15]. Nevertheless, the heavy use of these oxidants will produce extra sulfates or organic carbon and greatly increase additional processing costs. As an easily available oxidant, O<sub>2</sub> is one of the most abundant gas in air and does not contain other elements, which makes it act as a relatively inexpensive and green alternative to the above-mentioned oxidants. Among the numerous technologies developed for O<sub>2</sub> activation, heterogeneous photocatalysis is a prospective method due to the mild reaction condition and low energy cost [16–19]. However, because of the spin-forbidden

transitions, the photocatalytic conversion of O<sub>2</sub> into ROS suffers from low efficiency [20]. It is urgent to develop novel photocatalysts to drive the efficiency upgradation.

As a typical metal-free polymeric semiconductor, carbon nitride is considered as a promising photocatalyst due to the low environmental risk, facile molecular structure, and excellent physicochemical stability [21–23]. Limited by the inferior separation efficiency of photogenerated carriers and insufficient reactive sites, pristine carbon nitride commonly possesses poor photocatalytic performance. Introducing nitrogen vacancy (N<sub>V</sub>) is widely reported to be an effective approach to improve the photocatalytic performance of carbon nitride [24,25]. Nevertheless, single N<sub>V</sub> still exhibits a moderate efficiency as a result of the inadequate O<sub>2</sub> adsorption ability, which severely restricts the practical application.

Introducing additional reactive sites could address this issue to a large extent. Recently, constructing Brönsted acid sites in carbon nitride is demonstrated as efficient in improving the photocatalytic performance [26,27]. It is a reasonable hypothesis that Brönsted acid sites could enhance the O<sub>2</sub> activation on N<sub>V</sub> from two aspects: 1) Due to the low electronegativity of H atom in Brönsted acid site, the electron belonging to H atom will be extracted by N atom on carbon nitride and then flow into nearby N<sub>V</sub>, thus increasing the local electron density of N<sub>V</sub>

\* Corresponding author at: State Key Laboratory of Pollution and Resource Reuse, School of the Environment, Nanjing University, Nanjing 210023, PR China.

\*\* Corresponding author.

E-mail addresses: [13776501723@163.com](mailto:13776501723@163.com) (C. Zhu), [lfq@nju.edu.cn](mailto:lfq@nju.edu.cn) (F. Liu).

to boost the adsorption and activation ability for  $O_2$ . 2) The presence of H atom is conducive to the formation of N-H-N intramolecular hydrogen bonds in carbon nitride. This strong force may enhance the geometric stability of  $N_V$  when they interact with  $O_2$ , thus optimizing the  $O_2$  adsorption mode for better  $O_2$  activation. However, there is lack of facile method to fabricate Brönsted acid sites and  $N_V$  co-modified carbon nitride. The difficulty mainly lies in the introduction of Brönsted acid sites. In general, carbon nitride is prepared by the pyrolysis of small molecule precursors like cyanamide, urea and melamine. Because the H atom exists as  $-NH_2$  groups in these precursors, the H species is mainly present as hanging  $-NH_2$  groups or bridged  $-NH-$  groups after polymerization, resulting in carbon nitride obtained by direct pyrolysis being lack of Brönsted acid sites. To address it, subsequent operation like acid-treating and  $H_2$ -pyrolysis is necessary, which will bring extra inconvenience. By selecting appropriate precursors and pyrolysis procedure, introducing Brönsted acid sites along with  $N_V$  into carbon nitride is desired but challenging.

Inspired by these, with guanidinium thiocyanate as the precursor, this work successfully prepared Brönsted acid sites and  $N_V$  co-modified ultrathin carbon nitride nanosheets (UCN-H) through a facile two-step pyrolysis process. Detailed structural characterizations were conducted to probe the presence of Brönsted acid sites and  $N_V$  as well as their influences on the light adsorption and  $e^-h^+$  separation. The photocatalytic  $O_2$  activation and tetracycline (TC, a common antibiotic as the model pollutant) degradation performances were systematically evaluated. Quenching experiments and electron spin resonance (ESR) analyses were conducted to identify the dominated reactive species for TC degradation. The density-functional-theory (DFT) calculation was used to reveal the  $O_2$  adsorption behavior on  $N_V$  and the synergistic effect of Brönsted acid sites on neighboring  $N_V$  in converting  $O_2$  to ROS. The degradation pathway of TC was proposed and toxicity of intermediate products was also evaluated. Overall, this work could advance the mechanism understanding of  $O_2$  activation on dual-site carbon nitride and pave the way for the construction of green photocatalytic systems for efficient antibiotic wastewater treatment.

## 2. Materials and experiments

Details of chemicals, characterizations, photoelectrochemical measurements, DFT calculation, and toxicity prediction were provided in Text S1–6 in [Supplementary Material](#).

### 2.1. Preparation of photocatalysts

#### 2.1.1. Synthesis of bulk carbon nitride (BCN)

BCN was prepared by a simple pyrolysis method. 10 g of dicyandiamide (DCDA) was placed in the crucible with a cover, and then put in a muffle furnace heated for 4 h at 550 °C. The product was ground into yellow powder in the agate mortar.

#### 2.1.2. Synthesis of $N_V$ modified ultra-thin carbon nitride (UCN)

UCN was prepared by a simple thermal-etching method. A certain BCN was laid in the porcelain boat and then placed in the muffle furnace heated for 2 h at 550 °C. After natural cooling, the product was obtained.

#### 2.1.3. Synthesis of Brönsted acid sites modified bulk carbon nitride (BCN-H)

The same as the synthesis procedure of BCN with only guanidinium thiocyanate (GITC) to replace DCDA.

#### 2.1.4. Synthesis of Brönsted acid sites and $N_V$ co-modified ultra-thin carbon nitride (UCN-H)

The same as the synthesis procedure of UCN with BCN-H to replace BCN.

### 2.2. Photocatalytic experiments

All experiments were conducted on the photochemical reactor (XPA-7, Xujiang electromechanical plant, China) with a 500 W xenon lamp as the light source. During the reaction, a water-cooling system cooled the water-jacketed photochemical reactor to maintain the reaction temperature ( $25 \pm 0.5$  °C).

#### 2.2.1. Photocatalytic degradation experiments

In a typical experiment, 10 mg of catalyst was dispersed in 50 mL of TC solution ( $0.05 \text{ mmol L}^{-1}$ ). First, the suspension was stirred for 30 min to ensure the establishment of adsorption-desorption equilibrium before light irradiation. Afterwards, a 500 W xenon lamp was used as the light source. Within a predetermined irradiation time interval, 2 mL of suspension was extracted and centrifuged for further measurement by high performance liquid chromatography (HPLC).

To conduct the recycling experiments, after the reaction (illumination for 30 minutes), 2 mL of suspension was extracted and centrifuged for further measurement by high performance liquid chromatography (HPLC). And collected the used materials and rinsed with water and methanol for several times. The obtained materials were dried overnight for the next cycle experiments.

The degradation of ciprofloxacin (CIP,  $0.05 \text{ mmol L}^{-1}$ ), sulfamethoxazole (SMX,  $0.05 \text{ mmol L}^{-1}$ ), sulfamethazine (SMZ,  $0.05 \text{ mmol L}^{-1}$ ), norfloxacin (NFX,  $0.05 \text{ mmol L}^{-1}$ ) were also carried out by the same procedure to investigate the broad applicability of UCN-H.

#### 2.2.2. Photocatalytic quenching experiments

To investigate the main active oxygen species, quenching experiments were performed by adding tertiary butanol (TBA,  $100 \text{ mmol L}^{-1}$ ), nitroterazolium blue chloride (NBT,  $1 \text{ mmol L}^{-1}$ ), triethanolamine (TEOA,  $100 \text{ mmol L}^{-1}$ ) and furfuryl alcohol (FFA,  $100 \text{ mmol L}^{-1}$ ) to evaluate the possible contributions of  $\bullet OH$ ,  $\bullet O_2$ , photogenerated holes ( $h^+$ ) and  $^1O_2$  to TC degradation [28].

#### 2.2.3. Photocatalytic $\bullet O_2$ production experiments

Generally, 10 mg of catalysts were added in 50 mL of NBT solution ( $100 \mu\text{mol L}^{-1}$ ). The suspension was stirred for 30 min to ensure the establishment of adsorption-desorption equilibrium before light irradiation. Then, 2 mL of suspension was extracted and centrifuged for further measurement. As one NBT reacted with four  $\bullet O_2$  to produce purple insoluble formazan, the production amount of  $\bullet O_2$  could be estimated by the decrease amount of NBT [29].

## 3. Results and discussion

### 3.1. Morphology and structural characterizations

The morphology and microstructure of as-prepared photocatalysts were revealed by SEM and TEM images. Both BCN and BCN-H displayed a typical bulk-agglomerate structures (Fig. S2). Instead, as shown in Fig. 1a-b and Fig. 1d-e, both UCN and UCN-H indicated crooked layered-structures, which confirmed that the bulk structure was successfully exfoliated into layered structure during the second thermal-exfoliation process. The high angle annular dark field - scanning transmission electron microscope (HAADF-STEM) images and corresponding elemental mappings in Fig. 1c and f clearly showed that C and N elements were evenly distributed on the surface of UCN and UCN-H. According to the atomic force microscope (AFM) images, the thicknesses of UCN and UCN-H were measured as about 5.0 and 16.0 nm, respectively, further certifying the ultra-thin layered structure (Fig. 1g-h).

In the X-Ray Diffraction (XRD) patterns of prepared catalysts (Fig. 2a), the characteristic diffraction peak at  $27.8^\circ$  corresponded to the (0 0 2) crystallographic plane of carbon nitride. An obvious decrease of this diffraction peak in the XRD patterns of UCN and UCN-H could be observed, confirming that the thickness of carbon nitride was greatly

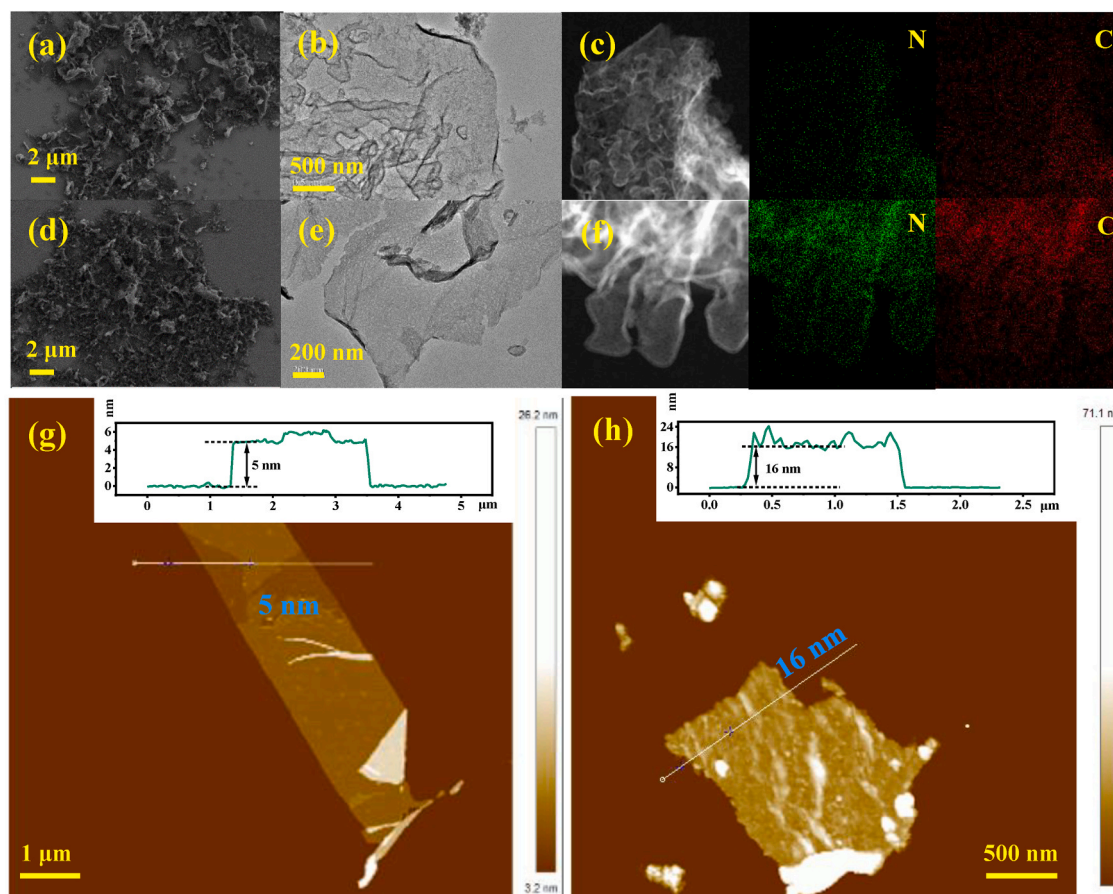


**Fig. 1.** (a) SEM image, (b) TEM image of UCN. (c) HAADF-STEM image and corresponding elemental mappings of UCN. (d) SEM image, (e) TEM image of UCN-H. (f) HAADF-STEM image and corresponding elemental mappings of UCN-H. (g) AFM images of UCN and UCN-H.

reduced during the second thermal-etching process [30]. As shown in Fig. 2b and Table S1, the specific surface area of UCN was determined as high as  $214.41 \text{ m}^2 \text{ g}^{-1}$ , which was 32.50 times higher than that of BCN ( $6.40 \text{ m}^2 \text{ g}^{-1}$ ), certifying the successful exfoliation of BCN. Similarly, the specific surface area of UCN-H ( $132.78 \text{ m}^2 \text{ g}^{-1}$ ) was also much higher than that of BCN-H ( $8.19 \text{ m}^2 \text{ g}^{-1}$ ). Because UCN-H was thicker than UCN, the specific surface area of UCN-H was lower than that of UCN. As depicted in Fig. S4a, the Fourier transform infrared spectroscopy (FTIR) spectra of as-prepared catalysts showed similar infrared absorption. The distinct peaks at  $800\text{--}820 \text{ cm}^{-1}$ ,  $1200\text{--}1600 \text{ cm}^{-1}$  and  $3000\text{--}3600 \text{ cm}^{-1}$  were attributed to the triazine units, aromatic C-N heterocyclic units and  $\text{-NH}_x$ , respectively, implying that the skeleton of carbon nitride was not seriously destroyed [31]. Notably, an obvious adsorption peak at  $815 \text{ cm}^{-1}$  could be observed from the magnified FTIR spectrum of UCN (Fig. S4b), corresponding to the breathing mode of heptazine units. However, the adsorption peak shifted to  $815 \text{ cm}^{-1}$  in the magnified FTIR spectrum of UCN-H, which indicated the strong intramolecular hydrogen bond in UCN-H [32].

In general, owing to the subtle difference of polymerization condition, carbon nitride obtained by thermal polymerization could be divided into melon CN and graphitic CN based on the polymerization degree (Fig. S5). The theoretical molecular formulas for melon CN and graphitic CN were  $\text{C}_3\text{N}_{4.5}\text{H}_{1.5}$  and  $\text{C}_3\text{N}_4$ , respectively. Based on the elemental analysis (EA) results in Fig. 2c and Table S2, the atom ratios of C, N and H in BCN, BCN-H, UCN and UCN-H were calculated as 3:4.57:1.79, 3:4.57:2.02, 3:4.57:1.92 and 3:4.53:2.20, respectively. Therefore, the as-prepared catalysts were melon CN. Moreover, it was found that the relative content of N decreased after the second thermal-exfoliation, indicating the formation of  $\text{N}_\text{V}$  in UCN and UCN-H. In addition, the UCN-H possessed more H atoms compared with UCN.

Generally, the N species in melon CN could exist as  $\text{-NH}_2$ , bridging  $\text{-NH-}$  or  $\text{C-NH=C}$  in heptazine ring. If the extra H atoms in UCN-H belonged to  $\text{-NH}_2$  and bridging  $\text{-NH-}$ , the N amount in UCN-H should be also proportionally higher than that in UCN. However, UCN-H and UCN exhibited similar N atom amounts, thus excluding the possibility of extra H atoms existing as  $\text{-NH}_2$  and  $\text{-NH-}$  forms. Considering the special structure of melon CN, the extra H atoms should be bonded with the  $\text{C-N=C}$  in heptazine ring, generating the well-known Brönsted acid sites, which would not result in the additional N amount increase. To further identify the existence of Brönsted acid sites, the in-situ pyridine adsorption was performed via FTIR (Fig. 2d). Two absorption peaks could be observed at  $1546$  and  $1640 \text{ cm}^{-1}$  in the spectrum of UCN-H (Fig. S6), indicating the existence of Brönsted acid sites [33]. Furthermore, based on the semi-quantitative results in Fig. 2e, the content of Brönsted acid sites on UCN-H ( $3.41 \mu\text{mol g}^{-1}$ ) was almost 4 times higher than that on UCN ( $0.71 \mu\text{mol g}^{-1}$ ). To further prove the presence of Brönsted acid sites, the solid-state nuclear magnetic resonance (NMR) spectra of UCN and UCN-H were also recorded. As shown in the  $^1\text{H}$  NMR spectra (Fig. 2f), both UCN and UCN-H exhibited the chemical shift at  $4.8$  and  $9.9 \text{ ppm}$ , corresponding to  $\text{D}_2\text{O}$  and  $\text{-NH}_x$  (including  $\text{-NH}_2$  and  $\text{-NH-}$  groups), respectively [34]. Additionally, a distinctly stronger signal at  $1.3 \text{ ppm}$  appeared in the  $^1\text{H}$  NMR spectrum of UCN-H, which was attributed to Brönsted acid sites.

X-ray photoelectron spectroscopy (XPS) was used to explore the surface element information. From the XPS survey spectra of BCN-H and UCN-H in Fig. S7, there was no signal of S element, indicating that S was completely released as gases during the polymerization process of GITC. As shown in Fig. 2g, the peak in the  $\text{N}1\text{s}$  spectrum of UCN at the binding energies of  $399.24$ ,  $400.83$  and  $401.75 \text{ eV}$  were ascribed to  $\text{C-N=C}$ ,  $\text{C-(N)}_3$  and  $\text{-NH}_x$ , respectively. As for UCN-H, the corresponding peaks



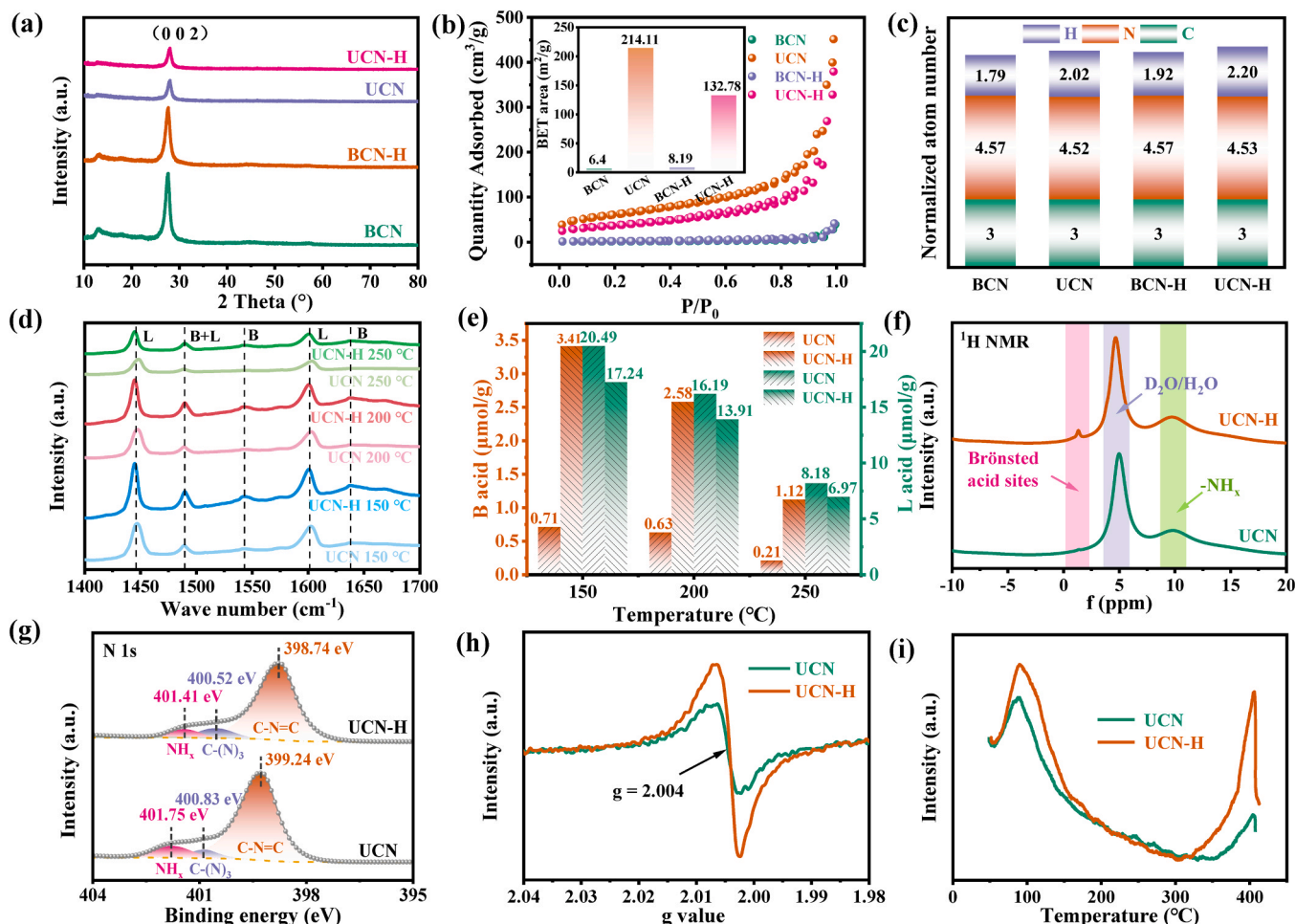


**Fig. 2.** (a) XRD patterns and (b)  $N_2$  adsorption-desorption isotherms of as-prepared samples. (c) Atom ratio of C, N and H in as-prepared samples (d) Pyridine-FTIR spectra of UCN and UCN-H (B and L refers to Brønsted acid sites and Lewis acid sites, respectively). (e) Amounts of Brønsted acid and Lewis acid in UCN and UCN-H under 150, 200 and 250 °C. (f)  $^1H$  NMR spectra, (g) N 1s XPS spectra, (h) Solid-state ESR spectra and (i)  $O_2$ -TPD profiles of UCN and UCN-H.

shifted to lower binding energies of 398.74, 400.52 and 401.41 eV, respectively. The C1s spectra of UCN and UCN-H exhibited similar tendency (Fig. S8). The characteristic peaks shifted to lower binding energy indicated higher electron density, which was attributed to the electron-donor effect of Brønsted acid sites [35]. The defective structure was further confirmed by the solid ESR analysis (Fig. 2h). The lorentzian line centered at the  $g$  value of 2.004 in UCN was associated with the single electron redistributed on the carbon atoms nearby  $N_V$ , confirming that the production of  $N_V$  during the second thermal-etching process [36]. Moreover, a stronger ESR signal was observed for UCN-H in relative to UCN, possibly due to the higher single electron density of  $N_V$  induced by Brønsted acid sites.  $N_V$  has been reported as an effective adsorption site for  $O_2$ . Then the  $O_2$  adsorption capacity of UCN and UCN-H was explored by  $O_2$ -temperature programmed desorption ( $O_2$ -TPD) measurement. As shown in Fig. 2i, the desorption peaks appeared around 90 and 390 °C in the  $O_2$ -TPD profile, corresponding to the physical adsorption and chemical adsorption of  $O_2$ , respectively. The higher peak intensity in the profile of UCN-H indicated the stronger  $O_2$  adsorption capacity.

### 3.2. Band structure and separation performance of photogenerated carriers

The band structures of as-prepared photocatalysts were determined by ultraviolet-visible diffuse reflectance spectra (UV-vis DRS) and XPS valance band spectra. As depicted in the UV-vis DRS (Fig. 3a), BCN-H

exhibited enhanced visible light adsorption compared with BCN, due to the  $n-\pi^*$  transition from Brønsted acid sites [37]. However, UCN and UCN-H displayed obviously weakened visible light adsorption, which was ascribed to the quantum size effect. It was worth noting that UCN-H showed an obvious red-shift in the UV-vis DRS compared with UCN, which indicated that the Brønsted acid sites could enhance the light adsorption ability. According to the Tauc-plots in Fig. S10, the energy bandgaps ( $E_g$ ) of BCN, UCN, BCN-H and UCN-H were calculated to be 2.80, 2.95, 2.78 and 2.86 eV, respectively. The valance band potentials ( $E_{VB}$ ) of BCN, UCN, BCN-H and UCN-H were 2.23, 2.31, 2.16 and 2.19 eV, which was evaluated by the XPS valance band spectra in Fig. S11. Then, the conduction band potentials ( $E_{CB}$ ) of BCN, UCN, BCN-H and UCN-H were determined as  $-0.57$ ,  $-0.64$ ,  $-0.62$  and  $-0.67$  V, respectively. The energy band structures of these samples were presented in Fig. 3b. As the  $E_{CB}$  values of these samples were all lower than the potential of  $O_2/\bullet O_2$  ( $-0.33$  V), all the catalysts could convert  $O_2$  into  $\bullet O_2$ .

The separation efficiency of photogenerated carriers was investigated by photoelectrochemical measurements. As shown in Fig. 3c, UCN-H exhibited the highest current response under simulated solar irradiation, which revealed the highest  $e^-h^+$  separation efficiency [38]. The electrochemical impedance spectra (EIS) in Fig. 3d showed that UCN-H possessed the smallest semicircle, suggesting the reduced migration resistance for photoexcited  $e^-$  in UCN-H [39]. To further study the migration property of photogenerated carriers, both the steady-state photoluminescence (PL) and transient-state PL measurements were



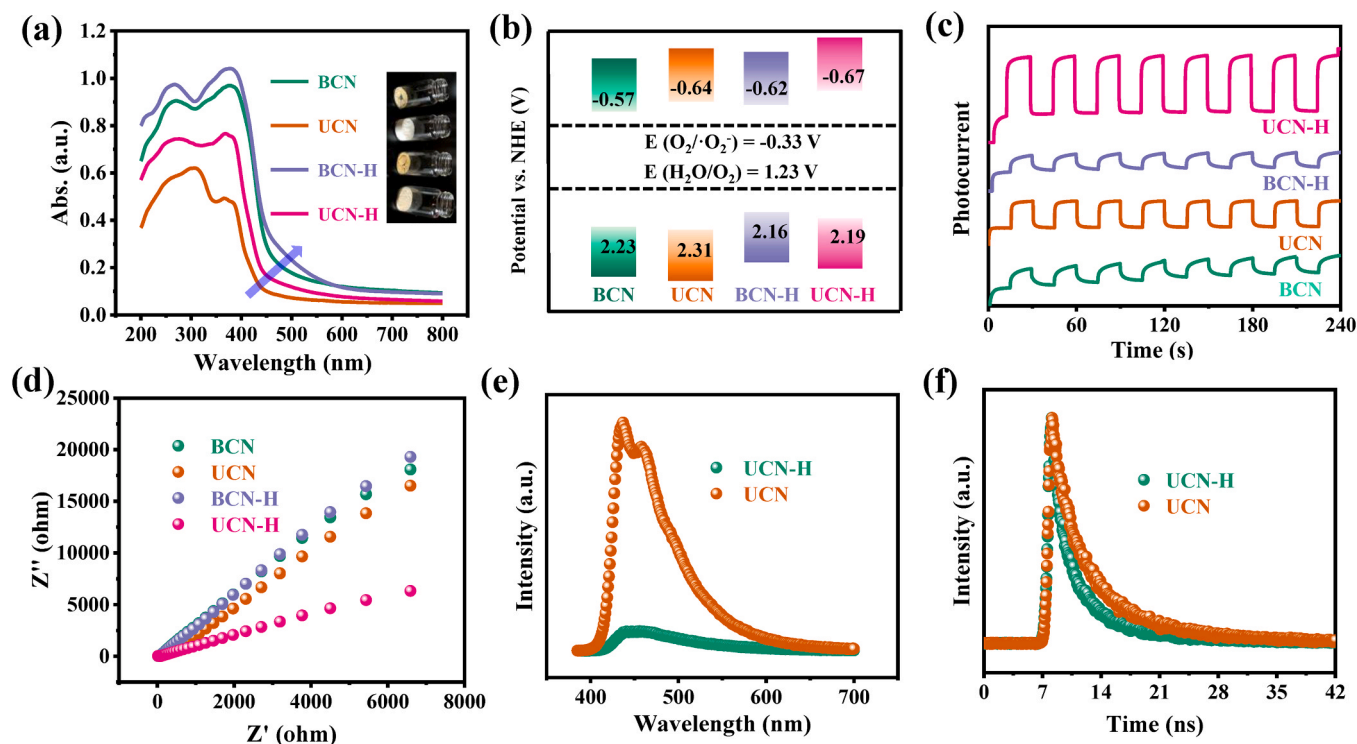


**Fig. 3.** (a) UV-vis DRS and (b) corresponding band structures of as-prepared samples. (c) PC curves and (d) EIS of as-prepared samples. (e) Steady-state PL spectra and (f) time-resolved PL decay curves of UCN and UCN-H.

operated. As shown in Fig. 3e, the PL emission intensity of UCN-H was much lower than that of UCN, which meant that the recombination rate of  $e^-h^+$  pairs in UCN-H was greatly suppressed. According to the PL decay spectra in Fig. 3f, the average fluorescent life of UCN-H was calculated as 6.67 ns, which was shorter than that of UCN-H (7.46 ns),

confirming the higher  $e^-h^+$  separation efficiency in UCN-H [40]. All of these measurements indicated that the introduction of Brönsted acid sites could effectively improve the light adsorption and  $e^-h^+$  separation.

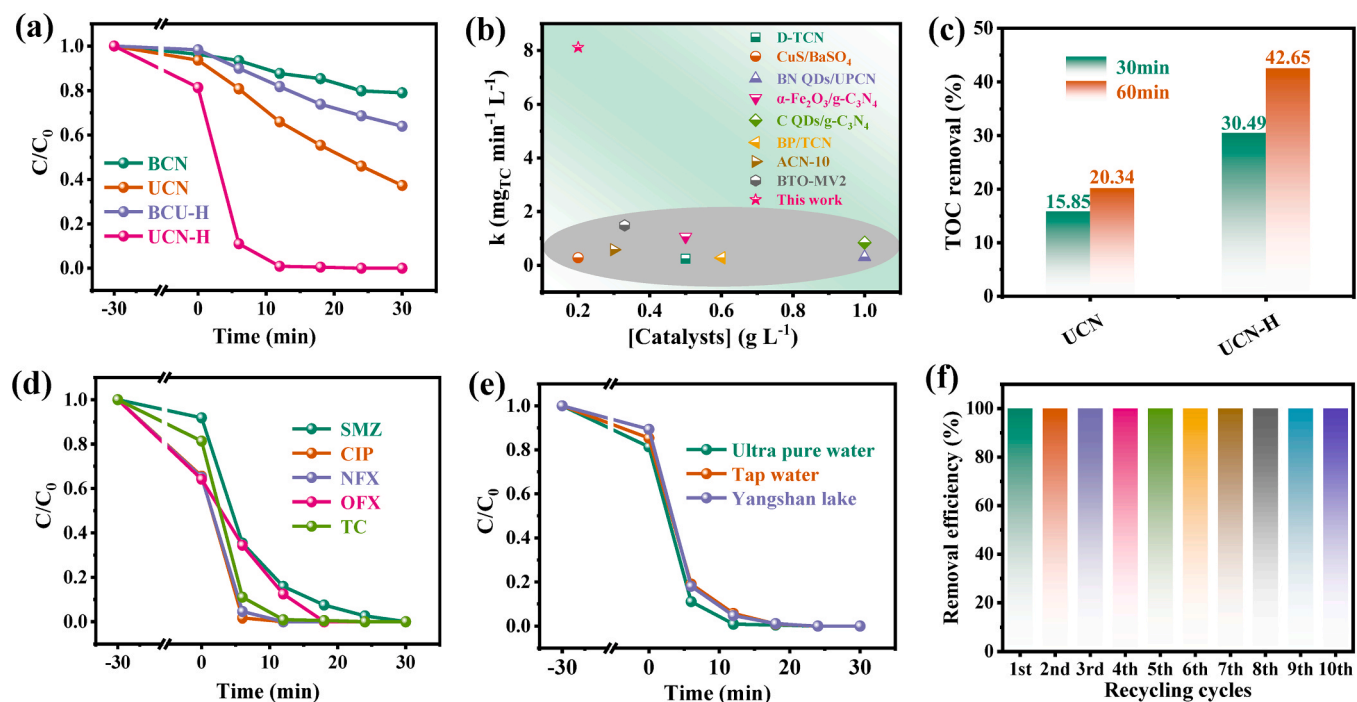


**Fig. 4.** (a) Time-dependent curves of photocatalytic TC degradation with as-prepared catalysts. (b) Comparison of TC degradation performance of UCN-H with those of reported photocatalysts. (c) TOC removal by UCN and UCN-H under different reaction times. (d) Time-dependent degradation curves of multiple antibiotics by UCN-H. (e) TC degradation efficiencies in different waters by UCN-H. (f) Cycle performance of UCN-H for photocatalytic TC degradation.

### 3.3. Photocatalytic performance

The photocatalytic activity of as-prepared photocatalysts was evaluated with TC as the model pollutant (Fig. 4a). BCN exhibited rather low TC degradation ratio (18.65% within 30 min), owing to the high recombination rate of  $e^-h^+$  pairs. For UCN, the TC degradation ratio increased to 62.56% within 30 min, indicating that the introduction of  $N_V$  could effectively enhance the photocatalytic activity. Further, UCN-H displayed the highest TC degradation ratio (100% within 18 min), and the corresponding kinetic rate constant ( $k_{obs}$ ,  $\text{min}^{-1}$ ) reached up to  $0.3783 \text{ min}^{-1}$ , which was 24.9 and 11.3 times higher than that of BCN-H ( $k_{obs} = 0.0146 \text{ min}^{-1}$ ) and UCN ( $k_{obs} = 0.0308 \text{ min}^{-1}$ ) respectively, suggesting that  $N_V$  and Brönsted acid sites could collectively promote TC degradation (Fig. S12a). Consideration the differences of specific surface areas, the specific surface area normalized degradation rates ( $k_n$ ,  $\text{min}^{-1} \text{ m}^{-2}$ ) was also calculated. As displayed in Fig. S12b, UCN-H still exhibited the highest normalized degradation rates than those of UCN and BCN-H, indicating the outstanding synergistic effect between Brönsted acid sites and  $N_V$ . Meanwhile, the photocatalyst-dose-normalized  $k$  value of UCN-H was  $41.613 \text{ mg g}^{-1} \text{ min}^{-1}$ , which surpassed those of reported photocatalysts by 8–130 times (Fig. 4b and Table S5) [19,20,41–46]. As depicted in Fig. 4c, for UCN-H, the total organic carbon (TOC) removal ratio was 42.65% within 60 min, which was higher than that of UCN (30.49%). Furthermore, UCN-H also possessed excellent degradation performance towards other antibiotics, including CIP, NFX, OFX and SMZ, with the degradation ratios all over 98% within 30 min (Fig. 4d).

The effects of initial pH and coexisting substances on TC degradation were investigated to evaluate the practical applicability of UCN-H. With the initial pH ranging from 3 to 11, there was no distinct fluctuation on TC degradation efficiency (Fig. S13a), indicating the high pH adaptability of UCN-H. The coexisting ions ( $\text{Cl}^-$ ,  $\text{SO}_4^{2-}$ ,  $\text{NO}_3^-$ ,  $\text{CO}_3^{2-}$  and  $\text{HPO}_4^{2-}$ )

and small molecular organic acids (Ethylene diamine tetraacetic acid, citric acid, oxalic acid, tannin acid and humic acid) exhibited little inhibition on TC degradation, indicating the excellent resistance to salinity and coexisting organics (Fig. S13b–c). The TC degradation in real water was also investigated (Fig. 4e). Only a weak suppression could be found in both tap water and Yangshan lake water, possibly due to the coexisting natural organic matters, ions or bacteria.

The reusability of UCN-H was evaluated in Fig. 4f. After 10 cycles of reuse, the TC degradation ratio maintained above 98%, indicating the excellent cycle performance of UCN-H. The durability of the catalyst was certified by several characterizations. As displayed in Fig. S14a–b, the used UCN-H could maintain the layered structure of fresh UCN-H. As showed in Fig. S14b, similar XRD patterns of fresh and used UCN-H could be found, indicating that the crystallographic structure of UCN-H remained unchanged after long-time usage. From the FTIR spectra of fresh and used UCN-H in Fig. S14d, the characteristic adsorption peaks of carbon nitride were still reserved. In addition, from the N 1 s and C 1 s XPS spectra in Fig. S14e–f, little shifts of binding energy were observed, implying the chemical state was steady during the reaction process. All the results confirmed that the durability of UCN-H was excellent.

### 3.4. Identification of reactive species

To explore the reactive species responsible for photocatalytic TC degradation, quenching experiments and ESR measurements were operated. Herein, TBA, NBT, FFA and TEOA were selected as the quenching agents for  $\bullet\text{OH}$ ,  $\bullet\text{O}_2$ ,  $^1\text{O}_2$  and  $h^+$ , respectively. Fig. 5a–b and Fig. S15 depicted the photocatalytic degradation curves of TC by UCN and UCN-H in the presence of different quenching agents. The addition of NBT significantly inhibited the degradation of TC with  $k$  value decreased from  $0.0308 \text{ min}^{-1}$  to  $0.0042 \text{ min}^{-1}$  for UCN and

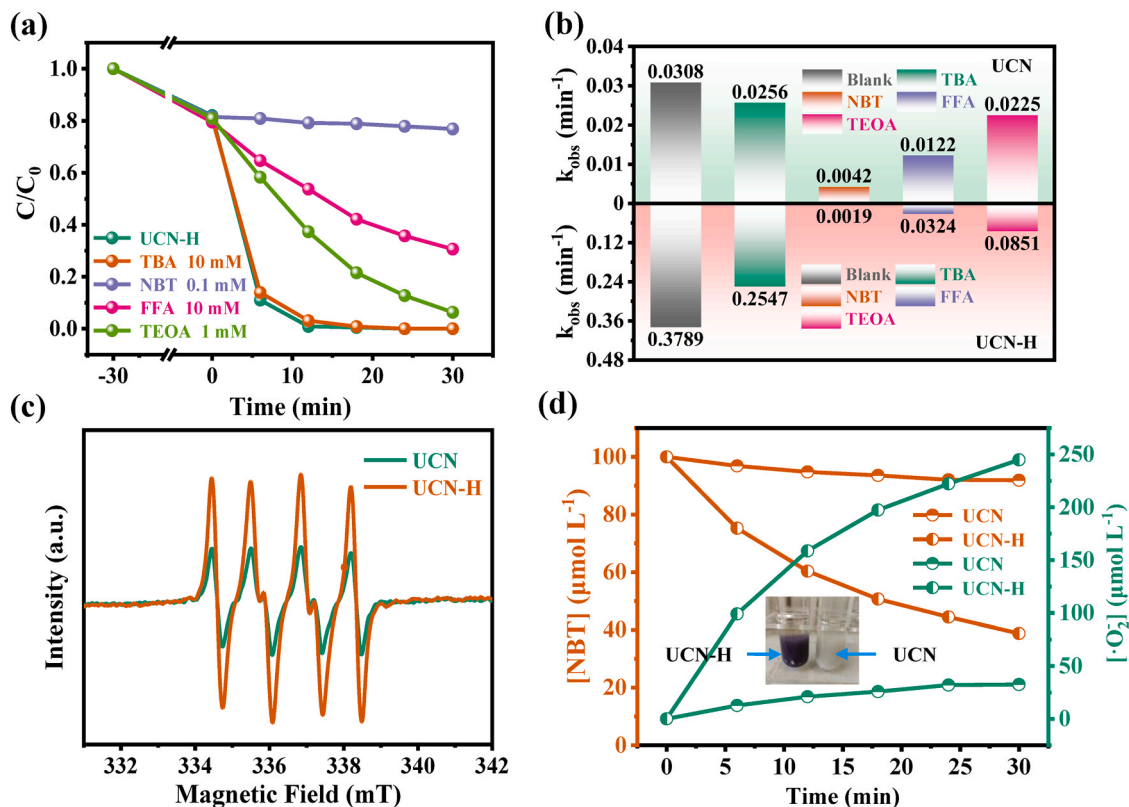


Fig. 5. (a) Time-dependent curves of photocatalytic TC degradation in the presence of different scavengers for UCN-H. (b)  $k$  values of TC degradation under adding different scavengers for UCN and UCN-H. (c) ESR spectra of DMPO- $\bullet\text{O}_2$  adduct for UCN and UCN-H. (d) Photocatalytic  $\bullet\text{O}_2$  production and NBT degradation profiles for UCN and UCN-H (Insert: Photograph of NBT solutions after photocatalysis for UCN and UCN-H).

0.3783 min<sup>-1</sup> to 0.0019 min<sup>-1</sup> for UCN-H, respectively, verifying the primary contribution of  $\bullet\text{O}_2^-$  to TC decomposition. The degradation of TC was also suppressed by FFA and TEOA, indicating that  $^1\text{O}_2$  and  $\text{h}^+$  might be involved in TC oxidation. There was negligible suppression on TC degradation after adding TBA, implying the insignificant contribution of  $\bullet\text{OH}$ .

The ROS generation on UCN and UCN-H was also monitored via ESR technique. As shown in Fig. 5c, under simulated solar irradiation, the ESR signal intensity of DMPO- $\bullet\text{O}_2^-$  adduct for UCN-H was much stronger than that for UCN, which indicated that UCN-H possessed higher  $\bullet\text{O}_2^-$  production capacity [47]. Furthermore, the accumulated  $\bullet\text{O}_2^-$  concentrations for UCN and UCN-H were determined via NBT degradation ratios in Fig. 5d. The accumulated  $\bullet\text{O}_2^-$  amount for UCN-H reached 244.92  $\mu\text{mol L}^{-1}$  within 30 min, which was 6.47 times higher than that of UCN (32.78  $\mu\text{mol L}^{-1}$ ). From the insert illustration in Fig. 5d, the obvious insoluble purple product was observed for UCN-H after reaction, implying the outstanding  $\bullet\text{O}_2^-$  production performance. Meanwhile, the ESR signal of DMPO- $\bullet\text{OH}$  adduct with the intensity ratio of 1:2:2:1 was also monitored for both UCN and UCN-H (Fig. S16). Based on the band structures in Fig. 3b, the  $E_{\text{VB}}$  values of UCN and UCN-H were measured as 2.31 and 2.19 V, respectively, which were lower than the standard redox potential of  $\text{H}_2\text{O}/\bullet\text{OH}$  (2.48 V), so both UCN and UCN-H couldn't oxidize  $\text{H}_2\text{O}$  to  $\bullet\text{OH}$ . In addition, quenching experiments also showed that  $\bullet\text{OH}$  was not the major reactive species. Hence, the detected ESR signal of DMPO- $\bullet\text{OH}$  should originate from the subsequent conversion of  $\bullet\text{O}_2^-$  (Eqs. 1–3). Besides, the characteristic ESR signal of TEMP- $^1\text{O}_2$  adduct was observed for both UCN and UCN-H. Based on previous researches,  $^1\text{O}_2$  in photocatalytic process could be generated through energy transfer or charge transfer. To identify the evolution path of  $^1\text{O}_2$ ,

NBT was used as the scavenger for  $\bullet\text{O}_2^-$ . A sharply reduced ESR signal intensity for TEMP- $^1\text{O}_2$  adduct was clearly found after NBT addition, suggesting that  $^1\text{O}_2$  was mainly derived from the oxidation of  $\bullet\text{O}_2^-$  (Eq. 4).



### 3.5. Synergy mechanism of Brönsted acid sites on $N_V$

From the above characterizations, UCN exhibited ultrathin layered structure with  $N_V$  on the surface, while UCN-H possessed both Brönsted acid sites and  $N_V$ . According to the normalized ratio of C and N, the as-prepared samples were melon CN. Therefore, DFT calculation was carried out on the basis of melon CN. As shown in Fig. S17, there were seven probable sites of  $N_V$  ( $N_{V1}$ ,  $N_{V2}$ ,  $N_{V3}$ ,  $N_{V4}$ ,  $N_{V5}$ ,  $N_{V6}$ , and  $N_{V7}$ ) on melon CN. Because the total energy of CN- $N_{V3}$  was calculated to be the lowest, the most possible configuration of UCN was determined as CN- $N_{V3}$ . On the basis of CN- $N_{V3}$ , the Brönsted acid site was further introduced into CN unite. There were two alternative probable sites positions to form the Brönsted acid site (Fig. S18a). As  $\text{H}_2\text{CN}-N_{V3}$  possessed a lower total energy, it was considered as the stable configuration of UCN-H (Fig. S18b-c).

With the determined configurations of CN, UCN and UCN-H, the energy band structures were calculated (Fig. 6a). For pristine CN, the  $E_g$

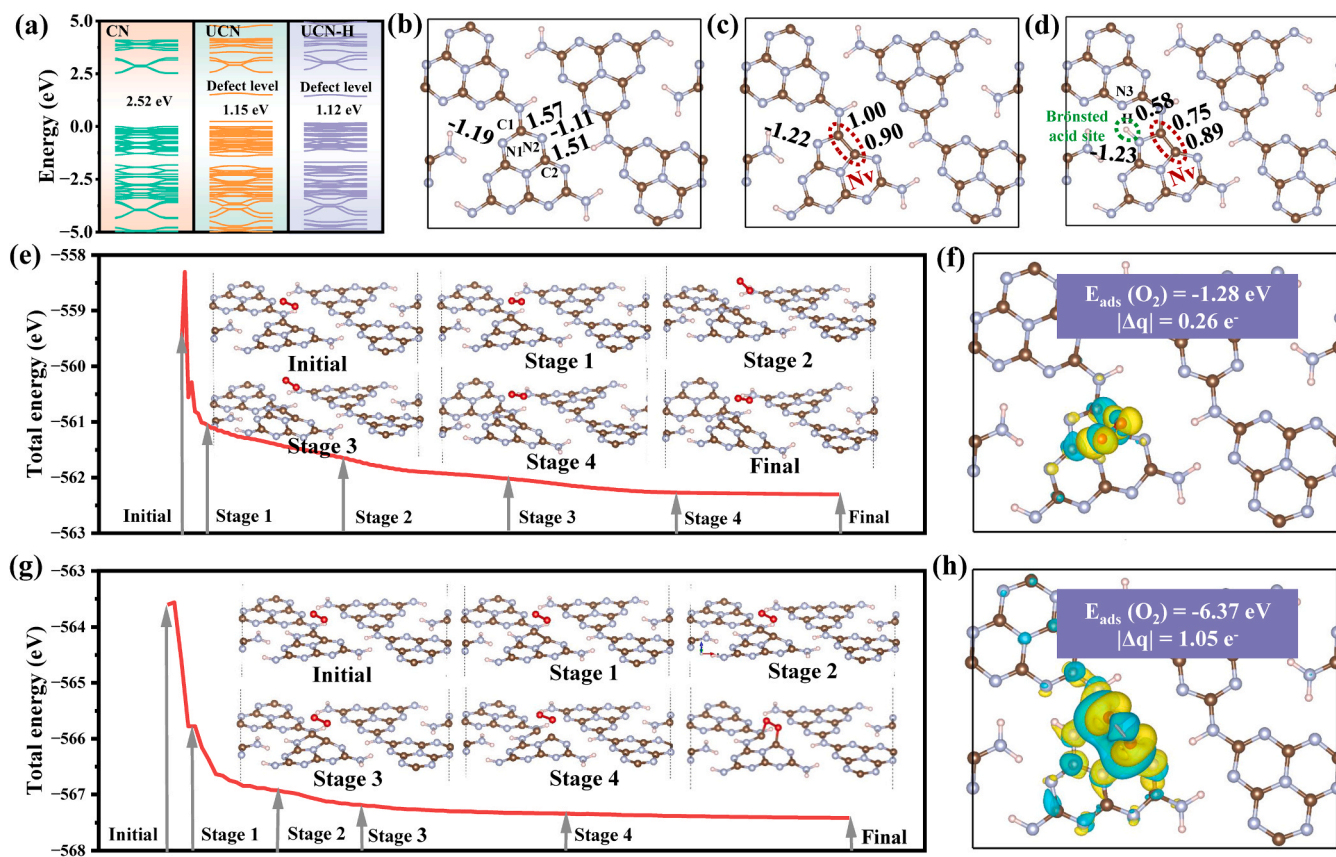


Fig. 6. (a) Band structures of CN, UCN, and UCN-H. (b) Optimized configurations of (b) CN, (c) UCN, and (d) UCN-H. (e) Variation of total energy during configuration optimization of  $\text{O}_2$  adsorption on UCN (Insert: Various configurations during the optimization process). (f) Calculated charge density difference for  $\text{O}_2$ -adsorbed UCN. (g) Variation of total energy during configuration optimization of  $\text{O}_2$  adsorption on UCN-H (Insert: Various configurations during the optimization process). (h) Calculated charge density difference for  $\text{O}_2$ -adsorbed UCN-H.



was 2.52 eV. However, after introducing  $N_V$  in CN, a distinct defect level appeared, making  $E_g$  decrease to 1.15 eV. The introduction of Brönsted acid site in UCN further narrowed the  $E_g$  to 1.12 eV. When the N atom was knocked out, the  $N_V$  was formed. Then the C atoms nearby the  $N_V$  closed to each other and formed a C-C bond. Hence,  $N_V$  was at the location of C1 and C2 atoms. The charge number of atoms around  $N_V$  in CN, UCN and UCN-H were shown in Fig. 6b-d. After knocking out N atom to form  $N_V$  in CN, the charge numbers of C1 and C2 atoms decreased from 1.57 and 1.51–1.00 and 0.90, respectively. Moreover, after introducing Brönsted acid sites into UCN, the charge numbers of C1 and C2 atoms further decreased to 0.75 and 0.89, respectively. In the meanwhile, the charge number of H atom was 0.58, demonstrating that H atom donated 0.58  $e^-$  to the nearby atom. Nevertheless, N1 atom possessed similar charge number before (−1.22) and after (−1.23) introducing Brönsted acid sites, indicating that electron density of N1 atom was steady. Based on the spatial positions of C1, C2, H, and N1 atoms, it was reasonable to infer that the donated electron from H atom flowed towards C1 and C2 atoms (i. e.  $N_V$ ) through N1 atom. The increased electronic density was beneficial to  $O_2$  adsorption and activation.

To investigate the effect of Brönsted acid sites on the  $O_2$  adsorption mode, the adsorption behavior of  $O_2$  on UCN and UCN-H was calculated (Fig. 6e and g). The  $O_2$  located on the C1 and C2 atoms in the bridging mode was assumed as the initial state. After structure optimization,  $O_2$  was adsorbed on the C2 atom of UCN in a side-on mode, while  $O_2$  maintained the bridging mode on UCN-H. These results indicated that introducing Brönsted acid sites could regulated the adsorption configuration of  $O_2$ . To understand how the difference between  $O_2$  adsorption modes was generated after introducing Brönsted acid sites, the configuration variation of both catalysts and  $O_2$  molecule during structure optimization was analyzed. For UCN, a macroscopic transformation occurred in the heptazine ring with  $N_V$  and the conjugated structure was

remarkably destroyed after the adsorption of  $O_2$ . The severe deformation influenced the  $O_2$  adsorption mode in turn. For UCN-H, due to the strong interaction of intramolecular hydrogen bond between the H atom in Brönsted acid site and nearby N3 atom, the heptazine ring with  $N_V$  kept super stability, thus avoiding the effect of substrate deformation on  $O_2$  adsorption. Therefore, only C1 and C2 atoms were drawn out of CN plane and the absorbed  $O_2$  maintained the bridging-adsorption mode with forming two strong C-O bonds for convenient electron transfer. In addition, as showed in Fig. S19, the C-C bond length was stretched to 1.76 Å after adsorbing  $O_2$ , which exceeded 1.6 Å (default value in the software), hence the bond was no longer displayed. The remarkable bond variation also indicated the strong interaction between  $O_2$  and  $N_V$ .

The  $O_2$  adsorption energies and charge density differences of different CN substrates were then calculated. For pristine CN, negligible  $O_2$  adsorption energy (−0.11 eV) was obtained, and the electron transfer amount from CN to  $O_2$  was only 0.014  $|e^-|$  (Fig. S20). As shown in Fig. 6f, after introducing  $N_V$  into CN, the adsorption energy for  $O_2$  increased to −1.28 eV, and the electron transfer amount increased to 0.26  $|e^-|$ . Moreover, with further introducing Brönsted acid site in UCN, the  $O_2$  adsorption energy and electron transfer amount increased to −6.37 eV and 1.06  $|e^-|$ , respectively (Fig. 6h). The highest  $O_2$  adsorption energy and largest electron transfer amount confirmed the strongest  $O_2$  activation ability of UCN-H.

### 3.6. Degradation pathway and toxicity prediction

The possible degradation products of TC were identified based on the ultra-performance liquid chromatography mass spectrometry (UPLC-MS) in Table S7. There were three possible degradation pathways of TC, as displayed in Fig. 7a. (I) Via the attack of reactive species, the demethylation reaction occurred on TC, and then P1 ( $m/z = 419$ ) was formed. Following the demethylation and dihydroxylation process, P2 ( $m/z =$

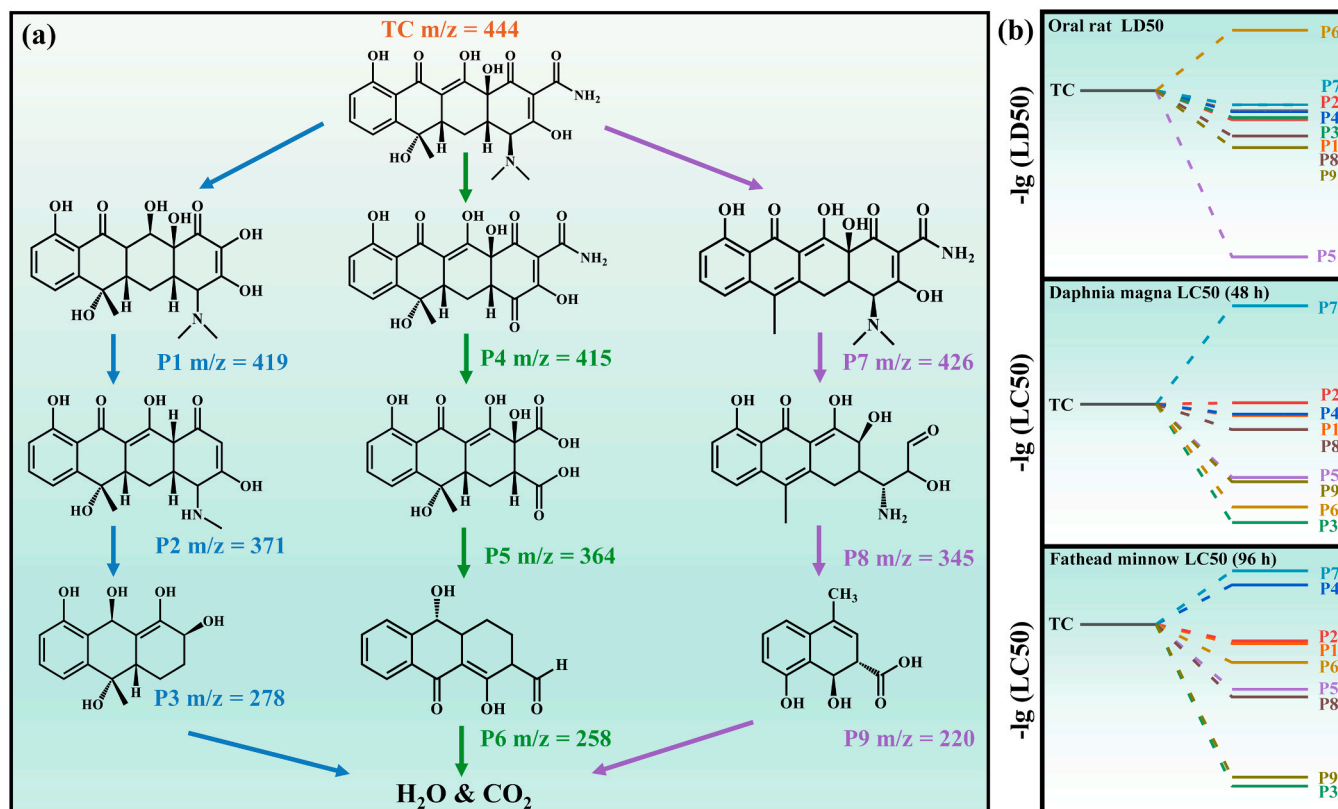


Fig. 7. (a) Proposed TC degradation pathways. (b) Fathead minnow PLC50 (96 h), Daphnia magna PLC50 (48 h) and oral rat PLD50 of TC and intermediate products.

371) was generated, which underwent ring opening to produce P3 ( $m/z = 283$ ). (II) Under the actions of  $\bullet\text{O}_2^-$ , the demethylation occurred on the amino group of TC firstly. Then P4 ( $m/z = 415$ ) was formed from the hydroxylation reaction, and P5 ( $m/z = 364$ ) was generated after deamidation and ring opening. Afterwards, P5 was attacked by reactive species to generate P6 ( $m/z = 258$ ). (III) By the attack of reactive species, hydroxylation reaction occurred on TC, and P7 was formed initially. After deamidation and ring opening reaction, P8 ( $m/z = 345$ ) was generated, and further decomposed into P9 ( $m/z = 220$ ) after ring opening reaction. After multiple ring-opening and dihydroxylation processes, P3, P6 and P9 were further degraded into small molecular organics,  $\text{CO}_2$  and  $\text{H}_2\text{O}$ . The acute toxicity of these intermediate products was estimated by Toxicity Estimation Software Tool (T.E.S.T.) (Fig. 7b). Generally, the acute toxicity of most intermediates (P1, P2, P3, P5, P8 and P9) were lower than that of TC. Some intermediates (P4, P6 and P7) exhibited increased. However, as most of the toxic intermediates were further degraded and even mineralized, their toxicity could be eliminated.

#### 4. Conclusion

In this work, the Brönsted acid sites and  $\text{N}_\text{V}$  co-modified ultra-thin carbon nitride (UCN-H) was successfully fabricated. The morphology and structure analysis as well as optical/electrochemical tests confirmed the presence of Brönsted acid sites and  $\text{N}_\text{V}$ , which could regulate the energy band structure and accelerate the  $\text{h}^+ \cdot \text{e}^-$  separation. Benefiting from the introduction of Brönsted acid sites, UCN-H exhibited exceptional degradation rate for TC ( $k_{\text{obs}} = 0.3783 \text{ min}^{-1}$ ), which was 11.3 times higher than that of UCN. Furthermore, UCN-H maintained high catalytic activity in a wide pH range of 3.0–11.0 and complex water matrix. DFT calculations revealed that Brönsted acid sites could not only increase the local electron density of  $\text{N}_\text{V}$ , but also improve the structure stability of  $\text{N}_\text{V}$  by forming intramolecular hydrogen bond, thus optimizing the  $\text{O}_2$  adsorption mode for enhanced  $\text{O}_2$  adsorption energy and electron transfer amount. Overall, this work paved the way for the construction of dual-site carbon nitride with synergistic effect to efficiently treat antibiotic wastewater via photocatalytic  $\text{O}_2$  activation.

#### CRediT authorship contribution statement

**Sun Nan:** Investigation, Data curation, Writing – review & editing. **Zhu Changqing:** Funding acquisition, Software, Writing – review & editing. **Liu Fuqiang:** Funding acquisition, Project administration, Writing – review & editing. **Yue Cailiang:** Conceptualization, Data curation, Investigation, Visualization, Writing – original draft, Writing – review & editing. **Zhu Linlin:** Data curation, Investigation, Visualization, Writing – review & editing. **Du Zhiling:** Writing – review & editing, Data curation.

#### Declaration of Competing Interest

The authors declare that they have no known competing financial interests or personal relationships that could have appeared to influence the work reported in this paper.

#### Data availability

No data was used for the research described in the article.

#### Acknowledgements

This work was supported by The National Key Research and Development Program of China (No. 2023YFE0100900), the National Outstanding Youth Science Fund Project of National Natural Science Foundation of China (No. 51522805) and the National Natural Science Foundation of China (No. 51908273).

#### Appendix A. Supporting information

Supplementary data associated with this article can be found in the online version at doi:10.1016/j.apcatb.2024.123860.

#### References

- [1] Y. Ahmed, J. Zhong, Z. Yuan, J. Guo, Simultaneous removal of antibiotic resistant bacteria, antibiotic resistance genes, and micropollutants by a modified photo-Fenton process, *Water Res.* 197 (2021) 498–508.
- [2] Z. Luo, R. Spinney, Z. Wei, W.-P. Hu, F.A. Villamena, W. Song, D.D. Dionysiou, R. Xiao, Reevaluation of the reactivity of superoxide radicals with a sulfonamide antibiotic, sulfacetamide: an experimental and theoretical study, *ACS EST Water* 1 (2021) 2339–2347.
- [3] Y. Ahmed, J. Zhong, Z. Wang, L. Wang, Z. Yuan, J. Guo, Simultaneous removal of antibiotic resistant bacteria, antibiotic resistance genes, and micropollutants by  $\text{FeS}_2/\text{GO}$ -based heterogeneous photo-Fenton process, *Environ. Sci. Technol.* 56 (2022) 15156–15166.
- [4] L. Tang, S. Zhou, F. Li, L. Sun, H. Lu, Ozone micronano-bubble-enhanced selective degradation of oxytetracycline from production wastewater: the overlooked singlet oxygen oxidation, *Environ. Sci. Technol.* 57 (2023) 18550–18562.
- [5] W. Hong, Y. Liu, T. Zhu, H. Wang, Y. Sun, F. Shen, X. Li, Promoting the catalytic ozonation of toluene by introducing  $\text{SO}_4^{2-}$  into the  $\alpha\text{-MnO}_2/\text{ZSM-5}$  catalyst to yune both oxygen vacancies and acid sites, *Environ. Sci. Technol.* 22 (2022) 15695–15704.
- [6] X.M. Xu, Y.M. Zhang, Y. Chen, C.H. Liu, W.J. Wang, J.J. Wang, H.T. Huang, J. Y. Feng, Z.S. Li, Z.G. Zou, Revealing  $\bullet\text{OOH}$  key intermediates and regulating  $\text{H}_2\text{O}_2$  photoactivation by surface relaxation of Fenton-like catalysts, *P. Natl. Acad. Sci.* 119 (2022) e2205562119.
- [7] X. Li, J. Hu, Y. Deng, T. Li, Z.-Q. Liu, Z. Wang, High stable photo-Fenton-like catalyst of  $\text{FeP}/\text{Fe}$  single atom-graphene oxide for long-term antibiotic tetracycline removal, *Appl. Catal. B: Environ.* 324 (2023) 122243.
- [8] F. Li, Z. Lu, T. Li, P. Zhang, C. Hu, Origin of the excellent activity and selectivity of a single-atom copper catalyst with unsaturated Cu- $\text{N}_2$  sites via peroxydisulfate activation:  $\text{Cu(III)}$  as a dominant oxidizing species, *Environ. Sci. Technol.* 56 (2022) 8765–8775.
- [9] Y. Zhao, L. Yu, C. Song, Z. Chen, F. Meng, M. Song, Selective degradation of electron-rich organic pollutants induced by  $\text{CuO}/\text{Biochar}$ : the key role of outer-sphere interaction and singlet oxygen, *Environ. Sci. Technol.* 56 (2022) 10710–10720.
- [10] H. Ming, P. Zhang, Y. Yang, Y. Zou, C. Yang, Y. Hou, K. Ding, J. Zhang, X. Wang, Tailored poly-heptazine units in carbon nitride for activating peroxymonosulfate to degrade organic contaminants with visible light, *Appl. Catal. B: Environ.* 311 (2022) 121341.
- [11] S. Wang, J. Wang, Single atom cobalt catalyst derived from co-pyrolysis of vitamin B12 and graphitic carbon nitride for PMS activation to degrade emerging pollutants, *Appl. Catal. B: Environ.* 321 (2023) 122051.
- [12] Y.-J. Sun, Z.-Y. Fang, X.-T. Huang, C.-W. Bai, K.-A. Zhu, X.-J. Chen, B.-B. Zhang, Y.-S. Zhang, Q. Yang, J.-X. Zheng, F. Chen, Efficient photo-switchable activation of periodate by nitrogen-vacancy-rich carbon nitride for organic contaminant removal: theoretical predictions and experimental validations, *Appl. Catal. B: Environ.* 337 (2023) 122994.
- [13] F. Liu, Z. Li, Q. Dong, C. Nie, S. Wang, B. Zhang, P. Han, M. Tong, Catalyst-free periodate activation by solar irradiation for bacterial disinfection: performance and mechanisms, *Environ. Sci. Technol.* 56 (2022) 4413–4424.
- [14] J. Kuang, H. Guo, Q. Si, W. Guo, F. Ma, Nitrogen vacancies regulated the local electron density of iron sites in  $\text{g-C}_3\text{N}_4$  to boost the generation of high-valent iron-oxo species in a peracetic acid-based Fenton-like process, *Appl. Catal. B: Environ.* 337 (2023) 122990.
- [15] Z. Wang, Z. Chen, Q. Li, J. Wang, L. Cao, Y. Cheng, S. Yu, Z. Liu, Y. Chen, S. Yue, J. Ma, P. Xie, Non-radical activation of peracetic acid by powdered activated carbon for the degradation of sulfamethoxazole, *Environ. Sci. Technol.* 57 (2023) 10478–10488.
- [16] D. Zhang, Y. Li, P. Wang, J. Qu, S. Zhan, Y. Li, Regulating spin polarization through cationic vacancy defects in  $\text{Bi}_4\text{Ti}_3\text{O}_{12}$  for enhanced molecular oxygen activation, *Angew. Chem.* 62 (2023) e202303807.
- [17] Y. Mao, P. Wang, L. Li, Z. Chen, H. Wang, Y. Li, S. Zhan, Unravelling the synergy between oxygen vacancies and oxygen substitution in  $\text{BiO}_{2-x}$  for efficient molecular-oxygen activation, *Angew. Chem. Int. Ed. Engl.* 59 (2020) 3685–3690.
- [18] C. Yang, S. Wan, B. Zhu, J. Yu, S. Cao, Calcination-regulated microstructures of donor-acceptor polymers towards enhanced and stable photocatalytic  $\text{H}_2\text{O}_2$  production in pure water, *Angew. Chem. Int. Ed. Engl.* 61 (2022) e202208438.
- [19] X. Xiao, Z. Ruan, Q. Li, L. Zhang, H. Meng, Q. Zhang, H. Bao, B. Jiang, J. Zhou, C. Guo, X. Wang, H. Fu, A unique  $\text{Fe-N}_4$  coordination system enabling transformation of oxygen into superoxide for photocatalytic C-H activation with high efficiency and selectivity, *Adv. Mater.* 34 (2022) e2200612.
- [20] L. Su, P. Wang, M. Li, Z. Zhao, Y. Li, S. Zhan, Synergistic enhancement of photocatalytic molecular oxygen activation by nitrogen defect and interfacial photoelectron transfer over Z-scheme  $\alpha\text{-Fe}_2\text{O}_3/\text{g-C}_3\text{N}_4$  heterojunction, *Appl. Catal. B: Environ.* 335 (2023) 122890.
- [21] S.P.J. John, T.P.D. Rajan, G.M. Anilkumar, T. Yamaguchi, S.C. Pillai, U.S. Hareesh, Graphitic carbon nitride ( $\text{g-C}_3\text{N}_4$ ) based heterogeneous single atom catalysts: synthesis, characterisation and catalytic applications, *J. Mater. Chem. A* 11 (2023) 8599–8646.

- [22] G.F.S.R. Rocha, M.A.R. da Silva, A. Rogolino, G.A.A. Diab, L.F.G. Noleto, M. Antonietti, I.F. Teixeira, Carbon nitride based materials: more than just a support for single-atom catalysis, *Chem. Soc. Rev.* 52 (2023) 4878–4932.
- [23] Y. Cui, X. An, S. Zhang, Q. Tang, H. Lan, H. Liu, J. Qu, Emerging graphitic carbon nitride-based membranes for water purification, *Water Res.* 200 (2021) 117207.
- [24] J. Cao, W. Nie, L. Huang, Y. Ding, K. Lv, H. Tang, Photocatalytic activation of sulfite by nitrogen vacancy modified graphitic carbon nitride for efficient degradation of carbamazepine, *Appl. Catal. B: Environ.* 241 (2019) 18–27.
- [25] L. Su, P. Wang, X. Ma, J. Wang, S. Zhan, Regulating local electron density of iron single sites by introducing nitrogen vacancies for efficient photo-Fenton process, *Angew. Chem. Int. Ed. Engl.* 60 (2021) 21261–21266.
- [26] B. Tahir, M. Tahir, N.A.S. Amin, Ag-La loaded protonated carbon nitrides nanotubes (pCNNT) with improved charge separation in a monolithic honeycomb photoreactor for enhanced bireforming of methane (BRM) to fuels, *Appl. Catal. B: Environ.* 248 (2019) 167–183.
- [27] C. Ye, X.-Z. Wang, J.-X. Li, Z.-J. Li, X.-B. Li, L.-P. Zhang, B. Chen, C.-H. Tung, L.-Z. Wu, Protonated graphitic carbon nitride with surface attached molecule as hole relay for efficient photocatalytic O<sub>2</sub> evolution, *ACS Catal.* 6 (2016) 8336–8341.
- [28] L. Ning, X. Chen, Z. Wang, J. Xu, High-efficiency pollutant degradation, disinfection and H<sub>2</sub>O<sub>2</sub> production activities of magnetically separable Co-imbedded N-doped carbonaceous framework/supramolecular perylene diimide photocatalyst, *Appl. Catal. B: Environ.* 324 (2023) 122282.
- [29] H. Wang, C. Yang, F. Chen, G. Zheng, Q. Han, A crystalline partially fluorinated triazine covalent organic framework for efficient photosynthesis of hydrogen peroxide, *Angew. Chem. Int. Ed. Engl.* 61 (2022) e202202328.
- [30] S. Li, B. Feng, X. Zhang, J. Tian, D. Wang, Y. Pei, M. Qiao, Y. Li, B. Zong, Multiple heteroatom-doped urea and thiourea-derived polymeric carbon nitride for high-performance visible light-driven photocatalytic O<sub>2</sub> reduction to H<sub>2</sub>O<sub>2</sub>, *Appl. Catal. B: Environ.* 335 (2023) 122879.
- [31] Z. Teng, Q. Zhang, H. Yang, K. Kato, W. Yang, Y.-R. Lu, S. Liu, C. Wang, A. Yamakata, C. Su, B. Liu, T. Ohno, Atomically dispersed antimony on carbon nitride for the artificial photosynthesis of hydrogen peroxide, *Nat. Catal.* 4 (2021) 374–384.
- [32] H. Lan, L. Li, X. An, F. Liu, C. Chen, H. Liu, J. Qu, Microstructure of carbon nitride affecting synergetic photocatalytic activity: hydrogen bonds vs. structural defects, *Appl. Catal. B: Environ.* 204 (2017) 49–57.
- [33] X. An, Q. Tang, H. Lan, H. Liu, X. Yu, J. Qu, H. Lin, J. Ye, Facilitating molecular activation and proton feeding by dual active sites on polymeric carbon nitride for efficient CO<sub>2</sub> photoreduction, *Angew. Chem. Int. Ed. Engl.* (2022) e202212706.
- [34] D. Zhao, Y. Wang, C.-L. Dong, Y.-C. Huang, J. Chen, F. Xue, S. Shen, L. Guo, Boron-doped nitrogen-deficient carbon nitride-based Z-scheme heterostructures for photocatalytic overall water splitting, *Nat. Energy* 6 (2021) 388–397.
- [35] Y. Deng, Z. Zhou, H. Zeng, R. Tang, L. Li, J. Wang, C. Feng, D. Gong, L. Tang, Y. Huang, Phosphorus and kalium co-doped g-C<sub>3</sub>N<sub>4</sub> with multiple-locus synergies to degrade atrazine: insights into the depth analysis of the generation and role of singlet oxygen, *Appl. Catal. B: Environ.* 320 (2023) 121942.
- [36] Y. Wang, D. Meng, X. Zhao, Visible-light-driven H<sub>2</sub>O<sub>2</sub> production from O<sub>2</sub> reduction with nitrogen vacancy-rich and porous graphitic carbon nitride, *Appl. Catal. B: Environ.* 273 (2020) 119064.
- [37] C. Fu, M. Zhao, X. Chen, G. Sun, C. Wang, Q. Song, Unraveling the dual defect effects in C<sub>3</sub>N<sub>5</sub> for piezo-photocatalytic degradation and H<sub>2</sub>O<sub>2</sub> generation, *Appl. Catal. B: Environ.* 332 (2023) 122752.
- [38] Y. Zhang, L. Cao, G. Bai, X. Lan, Engineering Single Cu Sites into covalent organic framework for selective photocatalytic CO<sub>2</sub> reduction, *Small* 19 (2023) 2300035.
- [39] Y. Liu, Y. Sun, E. Zhao, W. Yang, J. Lin, Q. Zhong, H. Qi, A. Deng, S. Yang, H. Zhang, H. He, S. Liu, Z. Chen, S. Wang, Atomically dispersed silver-cobalt dual-metal sites synergistically promoting photocatalytic hydrogen evolution, *Adv. Funct. Mater.* (2023) 2301840.
- [40] S. Li, R. Ma, S. Xu, T. Zheng, H. Wang, G. Fu, H. Yang, Y. Hou, Z. Liao, B. Wu, X. Feng, L.-Z. Wu, X.-B. Li, T. Zhang, Two-dimensional benzobisthiazole-vinylene-linked covalent organic frameworks outperform one-dimensional counterparts in photocatalysis, *ACS Catal.* 13 (2023) 1089–1096.
- [41] L. Chen, Y. Wang, S. Cheng, X. Zhao, J. Zhang, Z. Ao, C. Zhao, B. Li, S. Wang, S. Wang, H. Sun, Nitrogen defects/boron dopants engineered tubular carbon nitride for efficient tetracycline hydrochloride photodegradation and hydrogen evolution, *Appl. Catal. B: Environ.* 303 (2022) 120932.
- [42] Q. Chen, H. Zhou, J. Wang, J. Bi, F. Dong, Activating earth-abundant insulator BaSO<sub>4</sub> for visible-light induced degradation of tetracycline, *Appl. Catal. B: Environ.* 307 (2022) 121182.
- [43] W. Wang, Q. Niu, G. Zeng, C. Zhang, D. Huang, B. Shao, C. Zhou, Y. Yang, Y. Liu, H. Guo, W. Xiong, L. Lei, S. Liu, H. Yi, S. Chen, X. Tang, 1D porous tubular g-C<sub>3</sub>N<sub>4</sub> capture black phosphorus quantum dots as 1D/0D metal-free photocatalysts for oxytetracycline hydrochloride degradation and hexavalent chromium reduction, *Appl. Catal. B: Environ.* 273 (2020) 119051.
- [44] Y. Yang, G. Zeng, D. Huang, C. Zhang, D. He, C. Zhou, W. Wang, W. Xiong, X. Li, B. Li, W. Dong, Y. Zhou, Molecular engineering of polymeric carbon nitride for highly efficient photocatalytic oxytetracycline degradation and H<sub>2</sub>O<sub>2</sub> production, *Appl. Catal. B: Environ.* 272 (2020) 118970.
- [45] Q. Si, W. Guo, H. Wang, B. Liu, S. Zheng, Q. Zhao, H. Luo, N. Ren, T. Yu, Difunctional carbon quantum dots/g-C<sub>3</sub>N<sub>4</sub> with in-plane electron buffer for intense tetracycline degradation under visible light: Tight adsorption and smooth electron transfer, *Appl. Catal. B: Environ.* 299 (2021) 120694.
- [46] Y. Yang, C. Zhang, D. Huang, G. Zeng, J. Huang, C. Lai, C. Zhou, W. Wang, H. Guo, W. Xue, R. Deng, M. Cheng, W. Xiong, Boron nitride quantum dots decorated ultrathin porous g-C<sub>3</sub>N<sub>4</sub>: intensified exciton dissociation and charge transfer for promoting visible-light-driven molecular oxygen activation, *Appl. Catal. B: Environ.* 245 (2019) 87–99.
- [47] S. Wang, J. Zhu, T. Li, F. Ge, Z. Zhang, R. Zhu, H. Xie, Y. Xu, Oxygen vacancy-mediated CuCoFe/Tartrate-LDH catalyst directly activates oxygen to produce superoxide radicals: transformation of active species and implication for nitrobenzene degradation, *Environ. Sci. Technol.* 56 (2022) 7924–7934.